Advanced III/V quantum-structure devices for high performance infrared focal plane arrays

Robert Rehm[*a], Martin Walther[a], Johannes Schmitz[a], Frank Rutz[a], Joachim Fleissner[a], Ralf Scheibner[b], and Johann Ziegler[b]
[a]Fraunhofer-Institut für Angewandte Festkörperphysik, Tullastr. 72, 79108 Freiburg, Germany;
[b]AIM Infrarot-Module GmbH, Theresienstr. 2, 74072 Heilbronn, Germany

ABSTRACT

A mature production technology for Quantum Well Infrared Photodetector (QWIP) focal plane arrays (FPAs) and InAs/GaSb superlattice (SL) FPAs has been developed. Dual-band and dual-color QWIP- and SL-imagers are demonstrated for the 3-5 µm and 8-12 µm atmospheric windows in the infrared. The simultaneous, co-located detection of both spectral channels resolves the temporal and spatial registration problems common to existing bispectral IR-imagers. The ability for a reliable remote detection of hot CO_2 signatures makes tailored dual-color superlattice imagers ideally suited for missile warning systems for airborne platforms.

Keywords: QWIP, InAs/GaSb superlattice, MWIR, LWIR, infrared camera, dual-color, dual-band, carbon dioxide

1. INTRODUCTION

Although uncooled infrared (IR) detector technology based on thermal detectors and high operation temperature (HOT) photonic devices has shown significant progress in recent years, the need for cryogenically cooled IR photodetector arrays performing close to the theoretical limits remains.

Photodetectors for the atmospheric transmission windows in the mid-wavelength (3-5 µm, MWIR) and long-wavelength IR (8-12 µm, LWIR) are either based on small band gap direct semiconductors or semiconductor heterostructures. The most important and very common bulk compounds are InSb and $Cd_xHg_{1-x}Te$ (CMT). Both offer an excellent quantum efficiency and very large two-dimensional sensor arrays are available. While the cut-off wavelength in CMT can be adjusted by changing the alloy composition, InSb with its fixed band gap of 0.23 eV at 80 K lacks flexibility in this respect. CMT is usually grown epitaxially by liquid phase epitaxy (LPE) or molecular beam epitaxy (MBE). Common substrates are closely lattice matched CdZnTe or readily available Si- or Ge-wafers capped with appropriate buffer layers of a few microns thickness. Yet, even for MWIR CMT devices no substrate is known to date, which simultaneously satisfies all the necessities for being low-cost, lattice matched, chemically, optically and mechanically well suited. In the LWIR, the CMT band gap is very sensitive to the Cd mole fraction. Thus, the fabrication of large CMT arrays with a homogeneous performance becomes more and more challenging with increasing cut-off wavelength. Alternative approaches based on quantum-mechanically tailored semiconductor heterostructures offer the prospects to overcome these difficulties.

Quantum-Well Infrared Photodetectors (QWIPs) are III/V compound unipolar devices, in which the detection of infrared photons is based on resonant intersubband transitions in conduction band quantum wells [1]. In a typical n-type QWIP (see Fig. 1a), 20 - 50 periods of GaAs or $In_xGa_{1-x}As$ quantum wells separated by $Al_yGa_{1-y}As$ barrier layers are employed. The precisely controllable width and height of the resulting potential wells determine the total number and the energy of the subbands contained in each well. Most common are wells comprised of a ground state and one excited state at an energy approximately equal to the barrier height. The ground state in the conduction band is populated by appropriate n-

[*] Robert.Rehm@iaf.fraunhofer.de, phone (+49)-761-5159-353, fax (+49)-761-5159-400

Electro-Optical and Infrared Systems: Technology and Applications VI, edited by David A. Huckridge, Reinhard R. Ebert,
Proc. of SPIE Vol. 7481, 74810E · © 2009 SPIE · CCC code: 0277-786X/09/$18 · doi: 10.1117/12.835153

type doping of the wells. The absorption of resonant photons raises ground state carriers into the excited state. However, normal incident absorption is forbidden by a selection rule, which requires that the polarization of the incident radiation contains a component perpendicular to the layers. Specific grating couplers, which redirect the normal incident radiation of a backside-illuminated QWIP at a suited angle, are generally used to bypass the polarization selection rule.

Due to an applied electric field an excited carrier may preferentially leave the quantum well region and contribute to the photocurrent. Such a mobile carrier drifts along the field direction in the continuum above the barriers, but may also be captured in a subsequent well. Therefore, a photoconductive gain g, describing the ratio between the mean drift length and the thickness of the entire active layer, is associated with the transport process. For each generated mobile carrier the readout capacitor is charged with g electrons. Actually, a small gain is preferable under high photon flux conditions, e.g., in the LW, when only a readout integrated circuit (ROIC) with a limited charge storage capacity is at disposal [2].

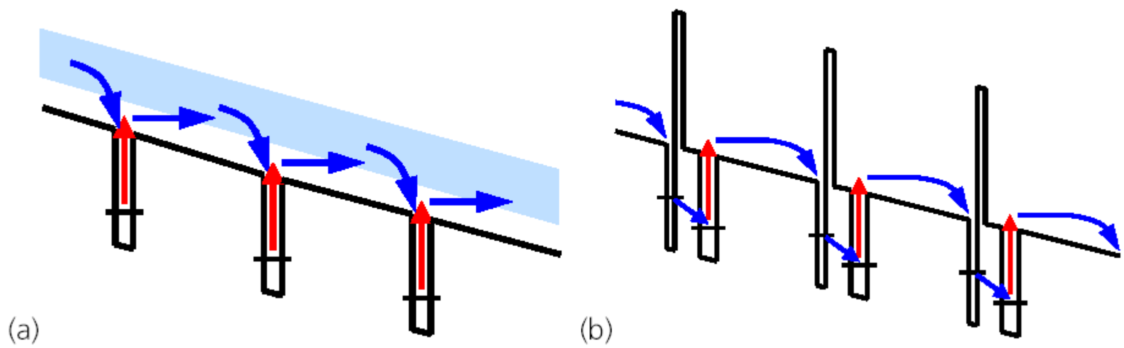

Fig. 1: Conduction band edge distribution and carrier transport mechanisms in a conventional photoconductive QWIP (a) and in a low-noise QWIP (b).

The photoconductive gain, i.e., the mean drift length, can be precisely controlled by the detector structure shown schematically in Fig. 1b [3]. Each period consists of four different zones, i.e., an excitation zone comprised of a doped quantum well, an AlGaAs drift zone, a capture zone realized with an undoped well and a tunneling zone including thin AlAs barriers. These barrier layers block very efficiently the carrier transport in the continuum and result in a deterministic recapture process after a carrier drift of exactly one period. Captured carriers reach the next period by a subsequent tunneling process. Hence, the noise associated with the recapture process in a standard photoconductive QWIP is eliminated and these structures are therefore called low-noise QWIPs. Compared to standard photoconductive QWIPs, low-noise QWIP focal plane arrays (FPAs) enable a higher dynamic range and improved thermal resolution [2].

Another very attractive quantum system are InAs/GaInSb short-period superlattices (SLs). In contrast to QWIPs, these antimony-based SL devices offer the potential for external quantum efficiencies comparable to CMT. The two materials form a broken gap type-II system, where the conduction band edge of InAs is lower in energy than the GaInSb valence band edge (see Fig. 2a). When both constituent's individual layer thickness is thin, an artificial band gap results on the basis of spatially separated electron and hole states in the InAs and GaInSb layers, respectively. The effective band gap can be adjusted from approximately 3-30 µm by altering the In mole fraction within the GaInSb and the individual layer thickness, which both can be precisely controlled during MBE growth. Typical values for the layer thickness of both materials in a single SL period range from 5-15 monolayers (ML) each. The coupling of neighboring electron wave functions leads to the formation of an electron miniband. Holes, however, are strongly localized within the GaInSb layers, which drastically reduces their mobility along the growth axis. The electron effective mass is significantly larger than in CMT and depends only weakly on the effective band gap. Tunneling contributions to the dark current are therefore reduced. The valence band structure can be adjusted such that non-radiative Auger recombination can be significantly reduced in p-type material. The minority electrons long lifetime, good vertical mobility and a high absorption coefficient result in a high quantum efficiency allowing short integration times and high frame rates.

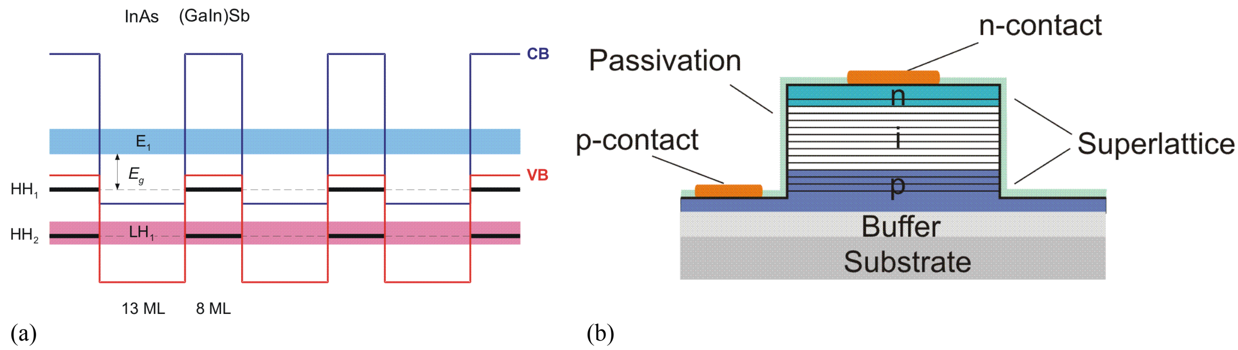

Fig. 2: (a) Schematic view of the type-II band structure alignment resulting in spatially indirect transitions in InAs/GaInSb superlattices. (b) Scheme of a mesa etched p-i-n SL photodiode.

For IR-detection purposes, photodiodes are generally realized by employing a p-i-n doping profile along the growth axis of the InAs/GaSb type-II superlattice (see Fig. 2b). The built-in electric field separates photogenerated carriers even without an externally applied bias voltage. To extract the photocurrent signal from the active area, the photodiode is sandwiched between ohmic n- and p-type contacts comprised of an appropriate combination of doped semiconductor material and a metallization sequence. These devices show broad-band absorption characteristics, where the long-wavelength cut-off is determined by the band gap of the superlattice and the short-wavelength cut-on is usually given by the spectral characteristics of the optical entrance window. Hence, these devices measure the integrated signal of a single wave band and are therefore referred to as monospectral detectors.

Similar to the transition from black-and-white to color photography in the visible spectral range, important information is revealed by accessing the spectral distribution of the infrared emission. Accordingly, both QWIP and InAs/GaSb SL technology have been pushed towards bispectral capability allowing to address two distinct IR wavelength bands on each pixel. A bispectral detector pixel is comprised of two detector stacks sandwiched between three contacts. The middle contact acts as common ground contact short-circuited externally by the ROIC. The three contacts per pixel allow to individually bias each channel and simultaneously integrate both signals. This approach allows for a perfect temporal and spatial registration of the spectral information even when the scene is changing rapidly.

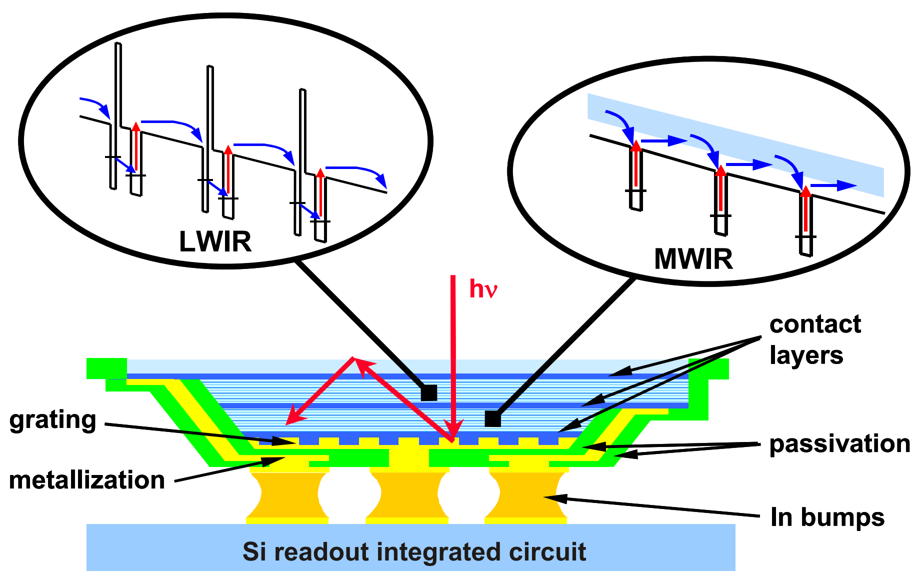

Fig. 3: Schematic cross-sectional view of a backside-illuminated dual-band QWIP pixel.

Bispectral FPAs operate either within two separate atmospheric windows (“dual-band”) or within the same transmission window (“dual-color”). Bispectral imaging provides several advantages like, e.g., remote absolute temperature measurement, operation in a wide range of ambient conditions, better distinction between target and background clutter and spectral discrimination of object features. Important IR imaging applications lie in the remote visualization of preselected gases like, e.g., carbon dioxide at 4.3 µm (see Fig. 4) or methane. Although, this can be accomplished using monospectral imagers in combination with selective filters, gas signatures can not be clearly distinguished from very hot, broad-band emitters like the sun, e.g., since the latter still provides very intense signals even after reflection on vegetation or sea. Bispectral imagers, however, measure the signal ratio between both bands for each imaged object. With this information, even for small, sub-pixel image sized objects, the distinction between a broad and narrow band emission can easily be automated.

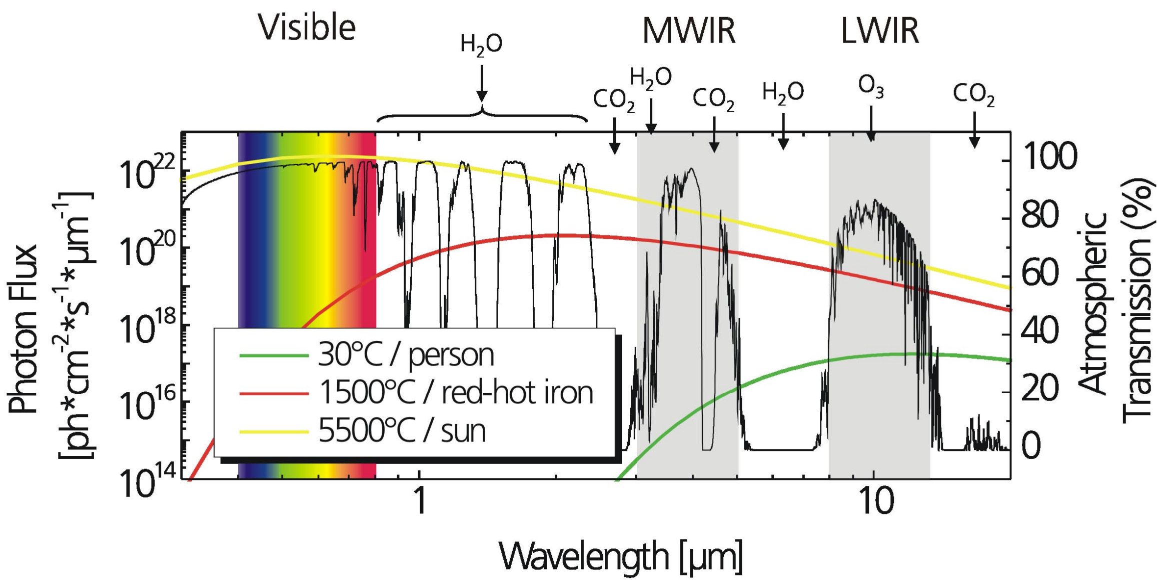

Fig. 4: Atmospheric transmission and electro-magnetic emission according to Planck’s law.

2. DUAL-BAND QWIP FOCAL PLANE ARRAYS

An ideal dual-band IR imager does not show any optical cross-talk between both channels. Contrary to broad-band absorbing CMT or antimony-based SLs, QWIPs with their characteristic narrow-band IR photoresponse (typical full width at half maximum ~10%) offer the important technological advantage to come close to this goal with comparatively thin active layers. In addition, QWIPs leverage the well established and cost-effective GaAs technology and they can be manufactured at very competitive prices with a close to perfect pixel yield. However, when a short-integration time is demanded by the particular application, QWIPs are not an ideal choice due to their limited external quantum efficiency (typically 10-20%).

At Fraunhofer-IAF, a fabrication process for 288x384 dual-band QWIP FPAs allowing simultaneous and pixel-registered detection has been developed. The growth of dual-band QWIP detector structures is performed by MBE on (100)-oriented, undoped, semi-insulating 3”-GaAs substrates. A lattice-matched AlAs/AlGaAs superlattice eliminates substrate related defects and serves as an etch stop layer for the wet chemical substrate removal after hybridization with the ROIC. Next, the undoped GaAs target layer for the isolation trench etching process is grown. The lower, LW sensitive detector structure is a 20 period low-noise QWIP sandwiched between two GaAs contact layers, each highly doped with 2×10^{18} cm^{-3} Si. The upper MW detector consists of 20 periods of 2.6 nm wide $In_{0.3}Ga_{0.7}As$ quantum wells, each well doped with 2.1×10^{12} cm^{-2} Si, and merely 24 nm wide $Al_{0.32}Ga_{0.68}As$ barriers. A highly doped (2×10^{18} cm^{-3} Si) GaAs layer acts as top contact layer. For the realization of the two-dimensional grating coupler a thin $Al_{0.32}Ga_{0.68}As$ etch stop layer

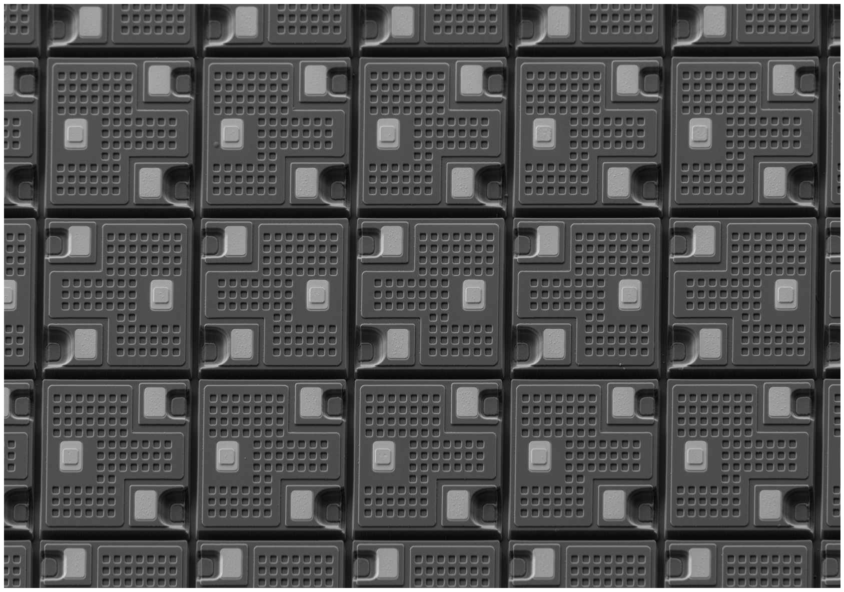

Fig. 5: SEM image showing a section of a dual-band QWIP FPA with 40 μm pixel pitch.

doped with 1.5×10^{18} cm^{-3} Si and 400 nm of 2×10^{18} cm^{-3} Si-doped GaAs terminate the dual-band detector structure. The contact layer in between the LW and the MW sensitive layers represents the common ground for both bands and is short-circuited externally by the ROIC.

In a full 3”-wafer process, 12 dual-band QWIP-FPAs each with 288x384 pixels at 40 μm pitch and a chip size of 16.1 mm x 12.1 mm are processed using standard optical lithography. Processing starts with the deposition of the upper ohmic contact metallization. Next, the two-dimensional grating coupler is etched on top of each pixel using a highly selective reactive ion etching (RIE) process. After several tests, a parameter set of 400 nm grating depth combined with a grating period of 2.85 μm, optimized to a peak wavelength of 8.5 μm, represented the best trade-off to achieve a similar noise equivalent temperature difference (NETD) within both bands. However, due to the significant area needed for the three contact lands and the large grating period, only a small number of grooves can be placed upon a dual-band pixel. This proved to degrade the coupling efficiency and broaden the spectral absorption characteristics. With chlorine-based chemically assisted ion beam etching (CAIBE) deep trenches for the electrical isolation of the pixels are realized. Subsequently, two wet chemical etching steps are employed to obtain both via holes for the common ground and the lower contact layer, respectively. After the deposition of a silicon nitride passivation layer, the passivation is selectively etched by a fluorine-based RIE process to get access to the semiconductor contact layers and a contact metallization pad is deposited. With the next layer a mirror reflector metallization is evaporated on top of the grating coupler and a short strip conductor between the metallization pads in the contact via holes and the corresponding contact lands on top of the pixels is formed. After the deposition of a second passivation layer and its selective removal, the front side process is completed by the evaporation of a final metallization layer required for the hybridization with the ROIC. Fig. 5 shows a Scanning Electron Microscopy (SEM) picture of a completely processed 288x384 dual-band QWIP-FPA with 40 μm pixel pitch.

After dicing the wafers into single chips, the detector arrays are hybridized to a custom-designed silicon ROIC by flip-chip re-flow indium soldering technology. The ROIC is optimized for high charge handling capacity using only two capacitors with equal storage capacity per unit cell and supporting simultaneous snapshot integration and individual bias control for both bands [4]. After hybridization, the GaAs substrate is completely removed by a combination of mechanical lapping and wet chemical etching. Since only single, free-standing pixels remain, thermally induced stress between the detector chip and the ROIC is eliminated and the optical cross talk between neighboring pixels is minimized. Fig. 3 schematically shows a cross sectional view of a dual-band QWIP-FPA pixel. The hybrid is finally mounted into a dewar and cooler assembly.

In addition to the detector arrays, each wafer contains various test devices to characterize the electrooptical performance. For the initial optimization of the coupling efficiency mesa structures of the same size as regular array pixels were included with a set of different grating parameters [5]. Also, mesas without grating of varying size are processed. The latter devices are exploited for the electrooptical standard characterization with 45° facet coupling. Fig. 6 shows the normalized photocurrent spectra of both bands with 45° facet coupling. At 77 K, the MW and LW bands show a 50%-cutoff wavelength of 5.1 µm (+1.0 V bias) and 8.7 µm (-1.0 V bias), respectively. The dark current densities at a typical operating bias of +1.0 V for the MW and –1.0 V for the LW are 3.4×10^{-7} A/cm^2 and 1.7×10^{-4} A/cm^2, respectively.

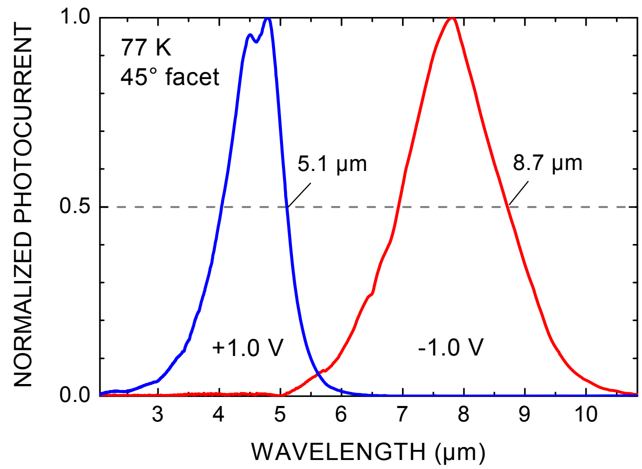

Fig. 6: Normalized photocurrent spectra of a dual-band QWIP measured with 45° facet coupling at 77 K.

The NETD of the 288x384 dual-band QWIP camera has been determined experimentally for a 300 K scene with F#/2.0 optics and 58 K detector temperature. Fig. 7 summarizes the results achieved with an integration time of 6.8 ms, which allows for a 100 Hz frame rate or a 2 × 2 microscan at 25 Hz for sub-pixel resolution (768 × 576 effective pixels). The gaussian fit function to the histogram data reveals excellent NETD values of 26.7 mK (MW) and 20.6 mK (LW), respectively. The pixel yield in both bands was lager than 99.5 %. Sample images of the 288x384 dual-band QWIP camera are shown in Fig. 10.

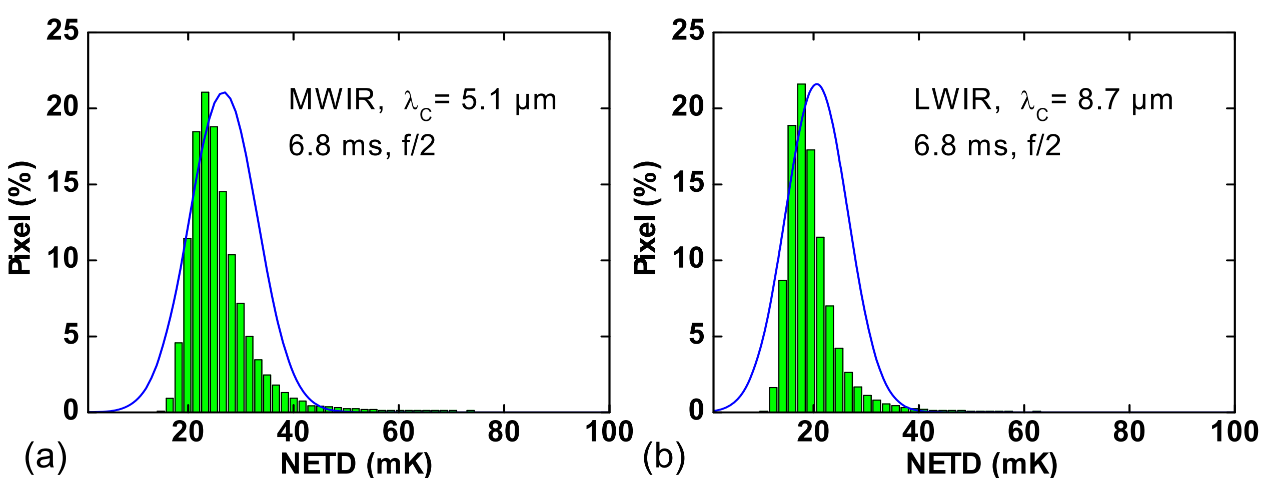

Fig. 7: NETD histograms of the MW (a) and LW (b) bands of a 288x384 dual-band QWIP camera at 58K.

3. DUAL-COLOR INAS/GASB SUPERLATTICE FOCAL PLANE ARRAYS

For bispectral imaging at 3-4 µm and 4-5 µm in the MWIR, dual-color InAs/GaSb SL FPAs have been developed [6]. The basic device concept resembles the dual-band QWIP approach described above. Two “back-to-back” InAs/GaSb SL p-i-n photodiodes are sandwiched between two n-type contacts and a common p-type ground contact externally short-circuited by the ROIC. By providing three electrical contacts on each pixel, a simultaneous, co-located detection of the “blue” (3-4 µm) and “red” (4-5 µm) channel is guaranteed.

The detector structures are grown in a 5 x 3" multi-wafer MBE system on (100)-GaSb substrates with 3” diameter. Standard group-III effusion cells for gallium, aluminum and indium and valved cracker cells for arsenic and antimony are used. N- and p-type doping of the superlattice regions and the contact layers is obtained using Si, GaTe and Be.

The layer structure starts with an isolating and lattice matched AlGaAsSb buffer layer followed by n-type doped GaSb. Next, a thick InAs/GaSb SL layer stack for the absorption of higher energy photons in the "blue channel” is grown. After growth of the pin-diode structure for the "blue channel", a common ground contact for both diodes is realized with a p-type GaSb layer. On top of the common ground contact, the diode structure for the “red channel” is grown followed by a 20 nm thick n-type InAs top layer.

The spectral cross-talk of the detector is mostly determined by the absorption of higher energy photons in the "red channel". Therefore, the thickness of the SL in the "blue channel" has to be rather thick in order to minimize spectral cross talk caused by high energy photons, which are not absorbed in the "blue channel". However, the process technology for mesa formation and contact via hole etching practically limits the thickness of the blue channel stack.

Dual-color FPAs on 3"-GaSb substrates with 288x384 detector elements and 40 µm pixel pitch are processed using optical stepper lithography. The processing starts with the formation of via holes to the common p-type contact layer followed by via hole etching to the n-type contact layer of the lower diode using a dry chemical etching process. The same process is also used to subsequently etch deep trenches for the electrical isolation of each pixel. After etching the via holes and the mesa trenches, the diodes are dielectrically passivated. In order to get access to the semiconductor contact layers, the passivation is partially opened with a reactive ion etching process. Afterwards, the contact metallization is evaporated to provide electrical contacts to the individual layer stacks. The metallization layer also serves as a mirror reflector on top of the backside illuminated FPA. After the deposition of several further metallization layers and an additional passivation layer, the front side process is completed. The SEM image in Fig. 8 shows a section of such a completely processed detector array. Each 3" wafer contains eleven dual-color FPAs with a chip size of 16.1 mm × 12.1 mm and a set of test dies for materials characterization.

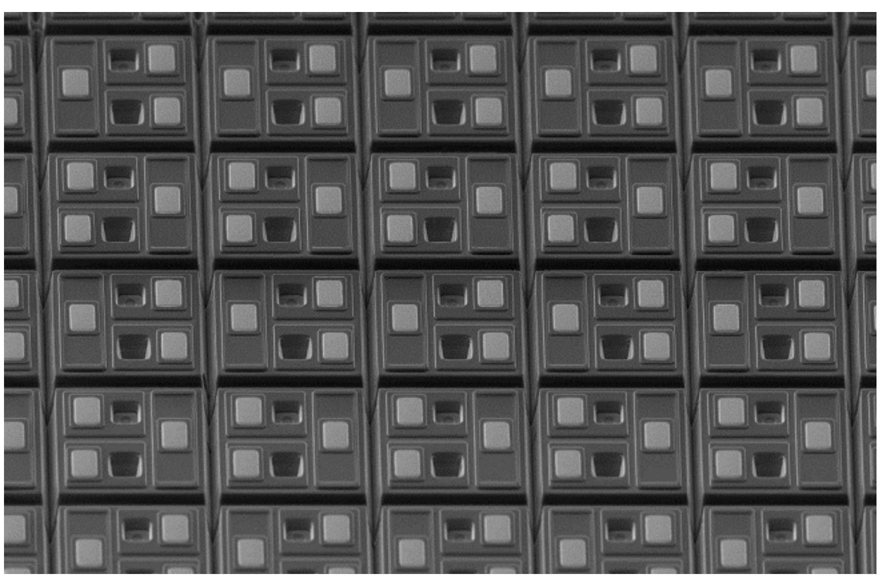

Fig. 8: SEM image showing pixels of a completely processed 288x384 InAs/GaSb SL dual-color FPA.

After completion of the front side process, the wafers are diced and the FPAs are flip-chip hybridized to a dual-color silicon ROIC with indium solder bump technology. To reduce the free carrier absorption in the substrate and to minimize the thermal stress between the dual-color detector chip and the silicon ROIC, the substrate is removed by a combination of mechanical lapping, polishing and wet chemical etching to a remaining thickness in the range of 20 µm.

After removal of the substrate, an anti-reflection coating is deposited on the illuminated detector side to lower reflection losses. Finally, the detector hybrid is placed on a ceramic sub-mount and mounted into an integrated detector cooler assembly (IDCA) equipped with a 1.5 W linear Stirling cooler. Now, the IDCA is electro-optically tested before it is further integrated up to a complete IR-camera module and comprehensive final acceptance tests are performed.

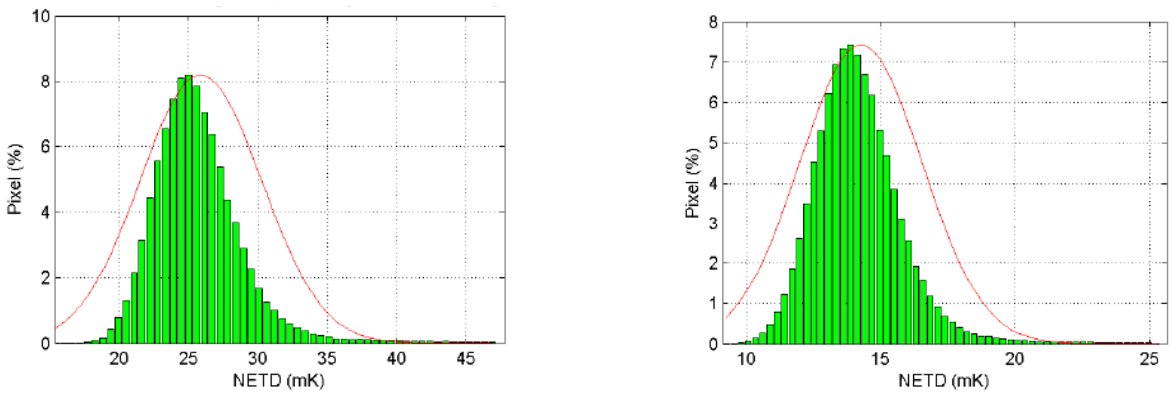

(a) (b)

Fig. 9: NETD histogram of a 288x384 InAs/GaSb SL dual-color camera measured at 78 K detector temperature and 0.2 ms integration time. (a) Blue channel (3-4 µm): <NETD> = 25.9 mK. (b) Red channel (4-5 µm): <NETD> = 14.3 mK.

Fig. 9 demonstrates the distribution of the NETD in both channels of a 288x384 InAs/GaSb SL dual-color IDCA measured without cold shield aperture at 78K detector temperature and 0.2 ms integration time. The mean NETD values resulting from a Gaussian fit of the histogram data are 25.9 mK and 14.3 mK for the blue and red channel, respectively.

Fig: 10: Bispectral IR-images of an industrial area. Cyan and red complementary RGB color scales have been used to fuse the blue and red detection channel of a dual-band QWIP- (upper image) and a dual-color SL-camera (lower image), respectively.

Fig. 10 compares two bispectral IR-images of an industrial area taken with a 288x384 dual-band QWIP camera (upper image) and a 288x384 dual-color SL camera (lower image), respectively. Two complementary colors, red and cyan, within the RGB color space were used to overlay the bispectral information. For the upper dual-band QWIP image the measured MWIR signal was supplied to the red RGB channel and the LWIR signal was fed into the cyan (= green + blue) RGB channel. For the lower dual-color SL image the 4-5 µm signal was coded in red, while the 3-4 µm signal was provided in cyan. Parts of the scene where the signals measured in both channels are comparable appear in a grey tone. This is generally the case for broad-band emitting objects.

While the dual-band imager integrates over the entire MWIR window, Fig. 10 clearly shows that the dual-color SL imager is ideally suited for remote detection of the strong carbon dioxide line around 4.3 µm (compare Fig. 4). CO_2 signatures can be clearly distinguished from water aerosols, which predominantly appear in the 3-4 µm channel due to the strongly increasing Rayleigh scattering at shorter wavelengths. In contrast to the dual-band camera, the dual-color SL imager clearly separates very bright sun light reflections appearing on the tower in the left part of the scene from hot CO_2 signatures. This capability makes the InAs/GaSb dual-color SL detector ideally suited for missile approach warners. A reliable identification of a missile's CO_2 plume allows to vastly reduce the false alarm rate in such warners. It will therefore be a key component for missile warning systems.

4. CONCLUSION

Over the last years, mature III/V fabrication processes for quantum-structure IR-detection devices, like QWIP- and antimony-based SL detectors, have been developed. Both technologies posses their individual pros and cons and, in general, offer a great deal of flexibility in the detector design, such that both technologies can be optimized for particular applications. Advanced high-performance bispectral QWIP- and SL IR-imaging systems in the MWIR and LWIR spectral range have been demonstrated. The bispectral cameras detect both spectral channels simultaneously on the same pixel, such that temporal and spatial registration problems do not exist. Similar to our daily experience in the visual spectral range, color imagers in the infrared reveal selective information, which is not easily accessible by monochrome detectors.

ACKNOWLEDGREMENTS

The authors are grateful to M. Korobka, J. Niemasz, W. Luppold, H.Güllich, A. Wörl, R. Beißwanger, S. Kopta, L. Kirste, B. Raynor and M. Finck for assistance in detector processing and characterization. Project funding by the Federal Ministry of Defense is gratefully acknowledged.

REFERENCES

[1] B. F. Levine, J. Appl. Phys. 74, R1 (1993).
[2] H. Schneider, T. Maier, J. Fleissner, M. Walther, P. Koidl, G. Weimann, W. Cabanski, M. Finck, P. Menger, W. Rode, and J. Ziegler, Proc. Int. Symp. on Advanced Electronics for Future Generations – Secure Life Electronics, Tokyo, 11.-12.10.2005.
[3] H. Schneider, C. Schönbein, M. Walther, K. Schwarz, J. Fleissner, and P. Koidl, Appl. Phys. Lett. 71, 246 (1997).
[4] W. Cabanski, M. Münzberg, W. Rode, J. Wendler, J. Ziegler, J. Fleißner, F. Fuchs, R. Rehm, J. Schmitz, H. Schneider, and M. Walther, in *Infrared Technology and Applications XXXI*, edited by B. F. Andresen and G. F. Fulop, Proc. SPIE, vol. 5783, 340 (2005).
[5] H. Schneider, Th. Maier, J. Fleissner, M. Walther, P. Koidl, G. Weimann, W. Cabanski, M. Finck, P. Menger, W. Rode, and J. Ziegler, in *Semiconductor Photodetectors II*, edited by M. J. Cohen and E. L. Dereniak, Proc. SPIE vol. 5726, 35 (2005).
[6] R. Rehm, M. Walther, J. Schmitz, F. Rutz, J. Fleissner, R. Scheibner, and J. Ziegler, in *Quantum Sensing and Nanophotonic Devices VI*, Proc. SPIE vol. 7222, 7222 0T (2009).